Journal of the Korean Ceramic Society
Vol. 53, No. 3, pp. 282~287, 2016.

http://dx.doi.org/10.4191/kcers.2016.53.3.282

Na-Ion Anode Based on $Na(Li,Ti)O_2$ System: Effects of Mg Addition

Soo Hwa Kim, Dong-Sik Bae, Chang-Sam Kim*, and June Gunn Lee*,†

Department of Convergence Materials Science and Engineering, Changwon National University, Changwon 51140, Korea

**Center for Energy Convergence Research, Korea Institute of Science and Technology, Seoul 02792, Korea*

(Received March 2, 2016; Revised April 13, May 10, 2016; Accepted May 18, 2016)

ABSTRACT

This study involves enhancing the performance of the $Na(Li,Ti)O_2$ system as an Na-ion battery anode with the addition of Mg, which partially replaces Li ions. We perform both computational and experimental approaches to achieve a higher reversible capacity and a faster transport of Na ions for the devised system. Computational results indicate that the $Na(Li,Mg,Ti)O_2$ system can provide a lower-barrier path for Na-ion diffusion than can a system without the addition of Mg. Experimentally, we synthesize various $Na_z(Li_y,Mg_x,Ti)O_2$ systems and evaluate their electrochemical characteristics. In agreement with the theoretical study, Mg addition to such systems improves general cell performance. For example, the prepared $Na_{0.646}(Li_{0.207}Mg_{0.013}Ti_{0.78})O_2$ system displays an increase in reversible capacity of 8.5% and in rate performance of 13.5%, compared to those characteristics of a system without the addition of Mg. Computational results indicate that these improvements can be attributed to the slight widening of the Na-O_6 layer in the presence of Mg in the $(Li,Ti)O_6$ layer.

Key words : Sodium-ion battery, P2 phase, Mg substitution, DFT, Barrier energy

1. Introduction

Green electricity from solar and wind energy requires large-scale energy storage, and electrochemical systems such as Li-ion batteries appear to be an effective and promising solution.[1-3] Because Li-ion batteries can provide high efficiency as well as excellent energy density, it is common practice these days to use such batteries as rechargeable energy sources in small electronic devices, motors, and electric automobiles.[4,5] The relatively high price of Li-ion batteries, however, is a critical drawback, especially when we consider it for application to large-scale energy storage.[6,7]

Na-ion batteries have been considered as alternatives because of their low price and the abundance of Na resources; however, the energy density and efficiency of Na-ion batteries are lower than those of Li-ion batteries. It should be noted that the price of raw materials takes a higher priority when large-scale energy storage is concerned.[8-10] There have been reported several non-metallic anodes for Na-ion batteries operating at room temperature such as hard carbon,[11] $Na_2Ti_3O_7$,[12] P2-$Na_{0.66}(Li_{0.22}Ti_{0.78})O_2$,[13] etc. Here, P2 represents a hexagonal layered structure having transition metal (TM) layers, O layers in the sequence of ABBA, and Na layers in trigonal–prisms of 6 oxygen atoms (see Fig. 1; more details will follow in later section).

Hard carbon has high reversible capacity (240 mAh·g^{-1}) and excellent cycle characteristics, but, because most of its discharge takes place at low voltages of 0.0 ~ 0.1 V (vs. Na^+/Na), it has the problem of dendrite growth by Na precipitation, and thus causes safety problems such as thermal runaway.[11] $Na_2Ti_3O_7$, on the other hand, has a problem of shortened lifetime due to the large volume change associated with the insertion and extraction of Na ions.[12]

Study of the $Na_{0.66}(Li_{0.22}Ti_{0.78})O_2$ system has showed very promising aspects of the layered P2 system that can solve the above-mentioned drawbacks: its average redox voltage is 0.75 V, eliminating the possibility of Na precipitation; its volume change by insertion and extraction of Na ion is as low as 0.77%.[13] In addition, the study estimated that the apparent Na^+ diffusion coefficient is about 1 x 10^{-10} $cm^{-2}s^{-1}$ which is high enough to give fast charge and discharge capabilities. This fast diffusion of Na ions is attributed to the unique structure of $Na_{0.66}(Li_{0.22}Ti_{0.78})O_2$, in which Na ions occupy relatively spacious prismatic sites made of 6 oxygen atoms between $(Li,Ti)O_6$ octahedral layers.[14-16] However, because of the limited empty sites for the reversible insertion and extraction of Na ions in the Na layers, the theoretical capacity of this material is limited to only 106 mAh·g^{-1}.

In this study, we attempt to increase the reversible capacity of P2-$Na_{0.66}(Li_{0.22}Ti_{0.78})O_2$ by partially substituting Li with Mg; we also attempt to reduce the Na fraction to less than 0.66 (this corresponds to increasing the ratio of Na sites for discharge to a value higher than 0.34), which has never been reported. To evaluate the possibility of effecting such a change, we first take a computational approach based on DFT, and carry out experiments to confirm the results by synthesizing the phase and analyzing it in terms

†Corresponding author : June Gunn Lee
E-mail : gunn@kist.re.kr
Tel : +82-2-958-5471 Fax : +82-2-958-5479

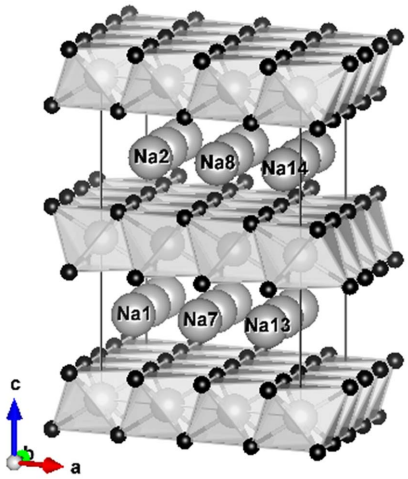

Fig. 1. Supercell model of P2 phase, $Na_{18}(Li_6Ti_{12})O_{36}$.

of reversible capacity and rate capability. Based on the results, we evaluate the effect of Mg addition and identify its role.

2. Experimental Procedure

2.1. Computational Study

We first performed DFT calculations on the Na_x(Li,Mg, Ti)O_2 systems to evaluate their transport properties and to provide theoretical support for the experiments. Calculations were carried out within the framework of density functional theory (DFT)[17] using the Vienna Ab-initio Simulation Package (VASP)[18] and MedeA-VASP.[19] We relaxed the electrons by projector augmented wave (PAW) potentials[20] with the exchange-correlation energy of the Perdew–Burke–Ernzerhof (PBE) parameterization[21] within the generalized gradient approximation (GGA).[22,23] We adopted Li(1s,2s,2p), Na(2p, 3s), Mg(2p, 3s), Ti(3d, 4s), and O(2s, 2p) orbital as valence states.

We used an energy cutoff of 500 eV and the gamma-centered scheme to generate a 2 × 2 × 2 k-point mesh (k-spacing = 0.5/Å). We confirmed the total energy convergence of less than 10^{-5} eV per atom and optimized the geometric structure using the conjugate gradient method until all forces fell below 0.02 eVÅ^{-1}. We did not consider spin polarization, dipole correction, or strong-correlation, because these factors do not affect the calculations of the energy differences in this case.

Table 1. Calculated Valence Charges and Charges Transferred Relative to Other Atoms by Bader Analysis

Atom	Valence Charge	Charge Transferred
Li	2.1088~2.1108	0.8892 ~ 0.8912
Mg	6.2857	1.7143
Ti	7.8469~7.8739	2.1261 ~ 2.1531
O	7.1296~7.3323	–1.3323 ~ –1.1296
Na	6.1359~6.1525	0.8641~0.8475

We used Bader analysis to calculate the electron transfer between atoms with the MedeA-VASP program.[19] For the barrier energy determinations, we employed the nudged elastic band (NEB) method using the VTST script[24] with 6 images including the initial and final configurations within a force convergence of less than 0.05 eVÅ^{-1}. In all systems in this study, the hexagonal geometry of the P2 phase was maintained. Illustrations related to these computational models are drawn using VESTA.[25]

Referring to previous studies,[15,16] we selected a reference model for this study as shown in Fig. 1. The structure belongs to the space group of $P6_3/mmc$ with hexagonal crystal system, and is a 3 × 3 × 2 supercell of $Na(Li_{0.33}Ti_{0.67})O_2$ in which each octahedron in the transition metal (TM) layer consists of Li or Ti atoms (light grey balls) at the center surrounded by 6 O atoms (small black balls). It should be noted that Na ions (big white balls) move along the inner-layer path which makes 2D diffusion possible. Based on this reference system, computational models were generated as shown in Table 1 by adding divalent Mg atoms to Li sites and/or by removing Na ions to create certain degrees of discharge.

Table 2 provides a summary of the Bader analysis which indicates the charge transferred for each constituting atom.

Table 2. Summary of Calculated Results for Four Computational Models of P2 Phase

System	Lattice Vectors (a, b, c, unit; Å) Supercell Volume (Å3)	Average Na-O length (Å) Na-O Prism volume (Å3)	Barrier Energy (eV)
$Na17(Li_6Ti1_2)O_{36}$	9.036 9.068 10.899	2.3981	0.462
	772.5230	12.8401	
Na17(Li5 Mg1Ti12)O36	9.040 9.072 10.916	2.4102	0.459
	774.3862	12.9919	
Na14(Li6Ti12)O36	9.030 9.031 11.031	2.4187	0.379
	774.48	12.9131	
Na14(Li5Mg1Ti12)O36	9.028 9.036 11.055	2.4244	0.341
	777.07	13.1188	

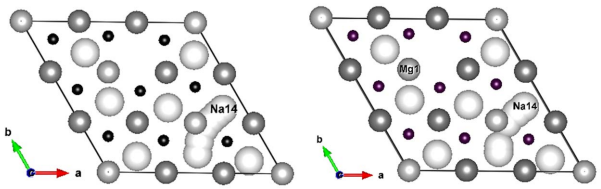

Fig. 2. Trajectories of Na#14 ion in $Li_6Ti_{12}O_{36}Na_{14}$ (left) and $Li_5Mg_1Ti_{12}O_{36}Na_{14}$ (right) systems during NEB simulations.

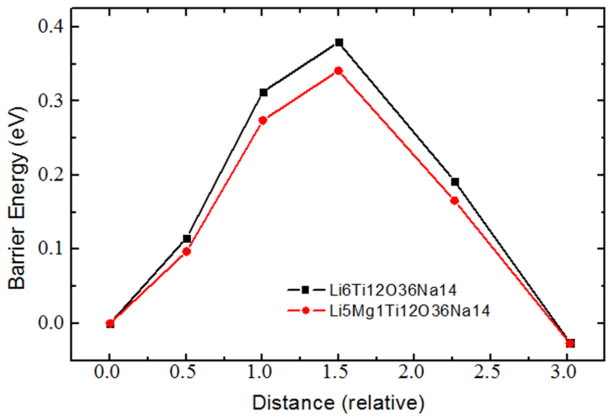

Fig. 3. Curves of energy barriers experienced by Na#14 ion when it moves from an initial site (marked as Na14) to an empty Na site (path length ≈ 3.1 Å) in $Li_6Ti_{12}O_{36}Na_{14}$ and $Li_5Mg_1Ti_{12}O_{36}Na_{14}$.

It should be noted that all the metals transfer electrons to O atoms and maintain local electroneutrality. Table 2 shows the four systems modeled for calculation; systems are 3 × 3 × 2 supercells of P2 phase with and without Mg in the TM layer. Each model corresponds to primitive P2 phase as follows: $Li_6Ti_{12}O_{36}Na_{17} \equiv Na[Li_{0.33}Ti_{0.67}]O2$, $Li_5Mg_1Ti_{12}O_{36}Na_{17} \equiv Na_{0.94}[Li_{0.278}Mg_{0.055}Ti_{0.67}]O_2$, $Li_6Ti_{12}O_{36}Na_{14} \equiv Na_{0.78}[Li_{0.33}Ti_{0.67}]O_2$, and $Li_5Mg_1Ti_{12}O_{36}Na_{14} \equiv Na_{0.78}[Li_{0.278}Mg_{0.055}Ti_{0.67}]O_2$. It should be noted that the models with 17 and 14 Na ions correspond to 82% and 35% of discharge, respectively.

The data conclusively confirm that the introduction of Mg ions into the TM layer of the P2 phase increases the lattice vector of the supercell along the c-axis, the average length of the Na-O bonds, and the average volume of the Na-O_6 prisms. These changes thus lead to ease of transport for Na ions, as indicated by the reduced barrier energies for the Mg-incorporated systems. It should be noted that this tendency is consistent for both high- and low-discharged cases, and also that Na ion transport becomes more difficult as the system is further discharged due to Na–Na repulsion.

Figure 2 shows, as examples, trajectories of the Na#14 ion in $Li_6Ti_{12}O_{36}Na_{14}$ and $Li_5Mg_1Ti_{12}O_{36}Na_{14}$ systems during NEB simulations; Fig. 3 provides curves of the energy barriers experienced by Na#14 ion when it moves from an initial site (marked as Na14) to an empty Na site (path length ≈ 3.1 Å).

2.2 Experimental

Raw materials for this study include Na_2CO_3 (Dae Jung Chem. ≥ 99.0%), Li_2CO_3 (Sigma Aldrich ≥ 99.0%), anatase TiO_2 (Sigma Aldrich ≥ 99.8%), and $MgCO_3$ (High Purity Chem. ≥ 99.9%). Table 3 shows the compositions considered and their theoretical capacities according to the various amounts of Li substituted with Mg. Each composition was prepared by mixing weighted raw materials with 250 ml of ethanol in a planetary mill (Fritsch, Pulverisette 5) with zirconia container and balls. The prepared slurries were dried in an evaporator, pressed into pellets, and heat-treated at 800, 850, 900, and 950°C for 20 h at heating rate of 5°C/min.

The heat-treated samples were analyzed by X-Ray Diffraction (Rigaku, D/MAX-2500V) at 40 kV, 100 mA, 5°~90°, step interval of 0.05°, and scan speed of 4°/min; phases were identified with JCPDS No. 52-0689 as the reference for the P2-$Na_{0.66}(Li_{0.22}Ti_{0.78})O_2$ phase. Microstructure was observed by scanning electron microscope (FEI, NOVA NanoSEM200).

Electrochemical cells were prepared with anodes of the $Na_x(Li_{y-z}Mg_zTi_{1-y})O_2$ system, cathodes of Na metal, and separators of glass microfibers. The anode samples were fabricated by mixing the synthesized anode powder, a conductive additive (Denka Black), and a binder (Polyvinylidenefluoride; PVdF 5 wt%) at a 8:1:1 weight ratio. The mixture was further mixed with NMP (1-methyl-2-pyrrolinone) to make the sample into paste form. The paste was casted on aluminum foil, dried, pressed, and punched into discs (φ12 mm) for use as anodes. The electrolyte consisted of 1 : 1 : 1 mol% of EC (ethylene carbonate), DEC (diethyl carbonate), and PC (propylene carbonate), with the addition of 1M $NaClO_4$. The electrochemical behavior of the prepared cells was characterized by static-current method in a WBCS3000 battery cycler (WonATech) at a 0.4~2.5 V range. The C-rate was varied from C/20 to 5C.

3. Results and Discussion

Figure 4 shows the XRD results for the $Na_{0.66}(Li_{0.22}Ti_{0.78})O_2$ sample in terms of the heat-treatment temperature. They indicate that the P2 phase formed at all temperatures. It should be noted that the peaks from the basal, prismatic,

Table 3. Compositions of P2 Phases Prepared for Anode and their Theoretical Capacity

Composition	Substitution Amount (%)	Theoretical Capacity (mAh g^{-1})
$Na_{0.66}(Li_{0.22}Ti_{0.78})O_2$	0%	106
$Na_{0.653}(Li_{0.214}Mg_{0.006}Ti_{0.78})O_2$	3%	108
$Na_{0.646}(Li_{0.207}Mg_{0.013}Ti_{0.78})O_2$	6%	111
$Na_{0.633}(Li_{0.194}Mg_{0.026}Ti_{0.78})O_2$	12%	115
$Na_{0.605}(Li_{0.165}Mg_{0.055}Ti_{0.78})O_2$	25%	124
$Na_{0.550}(Li_{0.11}Mg_{0.11}Ti_{0.78})O_2$	50%	141
$Na_{0.495}(Li_{0.055}Mg_{0.165}Ti_{0.78})O_2$	75%	159
$Na_{0.440}(Mg_{0.22}Ti_{0.78})O_2$	100%	177

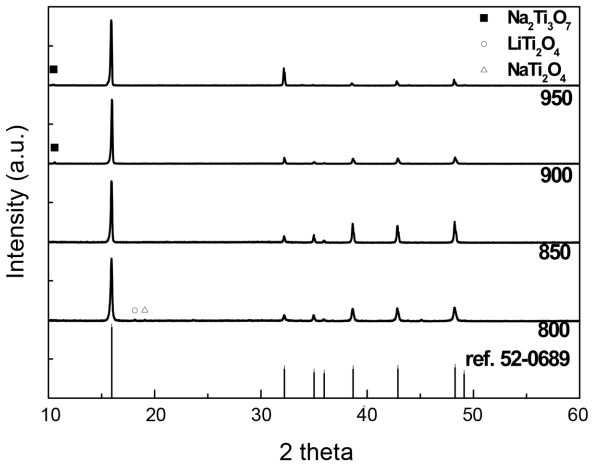

Fig. 4. XRD patterns of P2 phases at various heat-treatment temperatures.

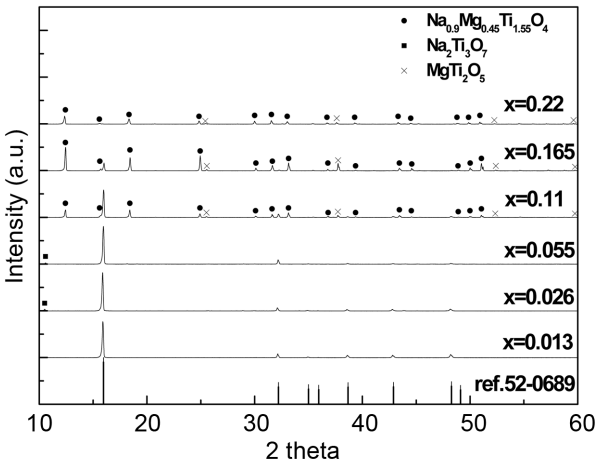

Fig. 6. XRD patterns of P2 and related phases with various values of x (see Table 4).

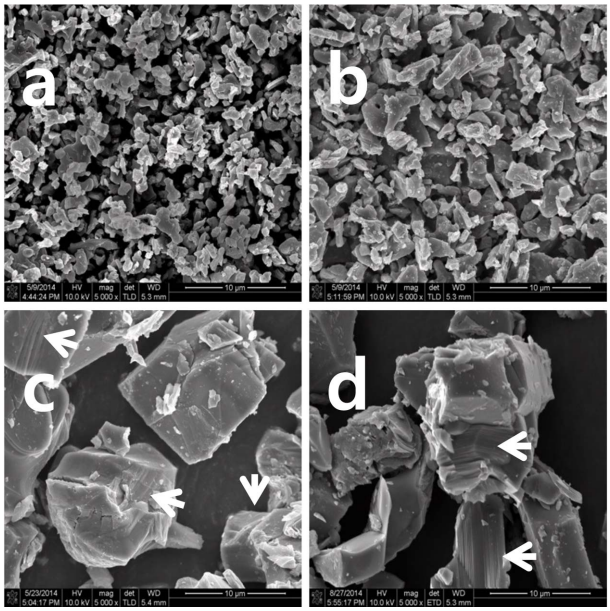

Fig. 5. SEM images of $Na_{0.66}(Li_{0.22}Ti_{0.78})O_2$ powders annealed for 20 h at (a) 800, (b) 850, (c) 900, and (d) 950°C.

and pyramidal planes of the P2 phase well developed up to 850°C. However, unintended peaks of $LiTi_2O_4$ and $NaTi_2O_4$ phases appeared at 800°C. At temperatures above 900°C, peaks other than those from the basal plane of P2 phase weakened rapidly, while peaks of the new $Na_2Ti_3O_7$ phase started to appear.

Figure 5 shows SEM images of the P2 phase. Powders prepared at 800 and 850°C show small (< 5 μm) and rounded grains, while those treated at temperatures higher than 900°C have grains bigger than 10 μm, are angular in shape, and have layers, as marked with the arrows. This could explain why peaks other than those from the basal plane of P2 phase weakened rapidly at this temperature.

Figure 6 shows the XRD results of the P2 phase in which part of the Li is replaced with Mg. These results indicate that the substitution takes place up to 0.013 mole of Mg, and can increase up to 0.055 mole of Mg with minor formation of $Na_2Ti_3O_7$ phase. Further substitution resulted in the formation of more secondary phases such as $Na_{0.9}Mg_{0.45}Ti_{1.55}O_4$ and $MgTi_2O_5$. The limit of Mg substitution is supposed to be less than 0.026 mole (actually 0.013 mole) in our experiment (From now on, we represent the degree of Mg substitution as x in unit of moles).

Figure 7 shows the results of the cycle test with a C-rate of less than 0.2C; results are summarized in Table 4. The best charge capacity and efficiency were found to result from the P2 phase, in which 0.013 mole of Mg is incorporated into the system. In this case, the initial charge capacity and efficiency at 0.05C improve by 8.5 and 7%, respectively, compared to the sample without Mg substitution. On the other hand, further substitution rather decreased both the charge and the discharge capacity, as well as the coulombic efficiency. The unintended substance $Na_2Ti_3O_7$ that appeared in the powders with 0.026 and 0.055 moles of Mg also is an active material. The average discharge and charge potentials of $Na_2Ti_3O_7$ are 0.2 and 0.4 V, respectively.[12] It was found that the $Na_2Ti_3O_7$ phase, however, did not work as an active material because the cutoff voltage was 0.4-2.5 V in this study. This may be one of the reasons for the lower capacity and coulombic efficiency of the powders with more than 0.013 mole Mg.

Figure 8 shows charge/discharge curves of the P2 phase with 0.013 mole of Mg and without Mg and shows that the P2 phase with 0.013 mole of Mg has a higher discharge potential and lower charge potential; these results are indicative of the lower overpotential during charge/discharge. This observation is in agreement with the lower barrier energy for Na diffusion, calculated by the DFT method for the P2 phase with Mg substitution.

Figure 9 shows the results of the charge/discharge capacity measured at a faster charge/discharge rate of up to 5C and 0.1C at the end. The P2 phase with Mg substitution

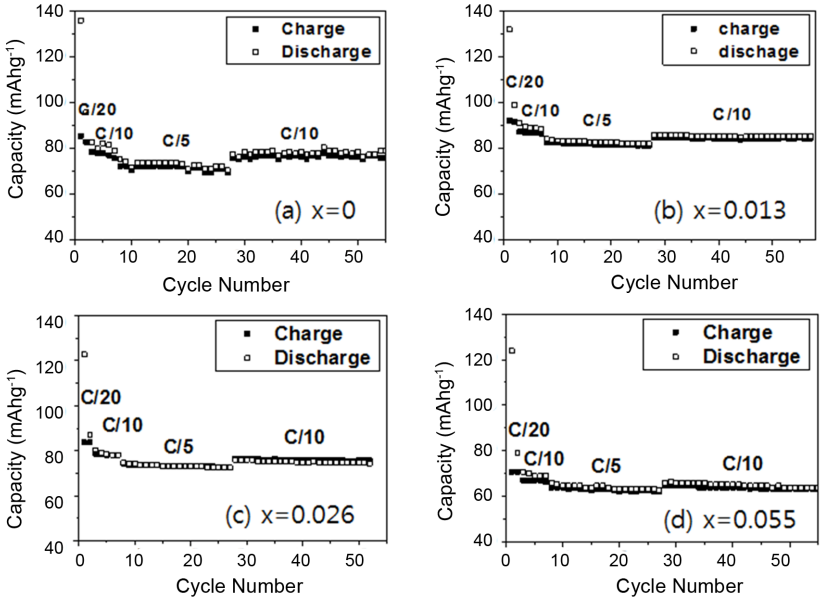

Fig. 7. Cycling behavior of P2 phases with various values of x (see Table 4).

Table 4. Average Charge Capacity at Various C-rates and Coulombic Efficiency for the First Cycle of P2-$Na_{0.66-x}(Li_{0.22}$-$xMg_xTi_{0.78})O_2$

x	C/20	C/10	C/5	Coulombic Efficiency (%)
0	85	78	72	63
0.013	92	87	83	70
0.026	84	79	74	68
0.055	71	67	64	57

maintains 77% of the initial capacity even at the faster charge/discharge rate of 5C, and fully recovers the initial capacity when the rate is reduced to 0.1C. This confirms that P2-$Na_{0.66}(Li_{0.22}Ti_{0.78})O_2$ is a very stable structure that undergoes only negligible volume change.

4. Conclusions

We prepare cells made of P2-type $Na_{0.66}(Li_{0.22}Ti_{0.78})O_2$ phase as anode and introduce Mg^{2+} into the transition metal layer to take the part of Li^+; this leads to a P2 phase with a Na ratio less than 0.66. The Mg-incorporated cells

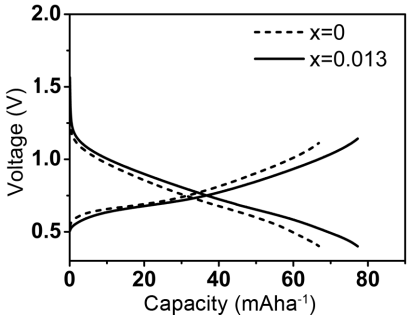

Fig. 8. Charge/discharge curves of P2 phases with x = 0 and 0.013 at C/2.

(0.013 ~ 0.026 mole of Mg) show a better electrochemical performance, as predicted by the first-principles calculation. Compared to the system without the addition of Mg, the prepared $Na_{0.646}(Li_{0.207}Mg_{0.013}Ti_{0.78})O_2$ system displays an increase in reversible capacity of 8.5% and an increase in rate performance of 13.5% at 1C. Computational results indicate that these improvements can be attributed to the widening of the Na layer by the presence of Mg in the $(Li,Ti)O_6$ layer.

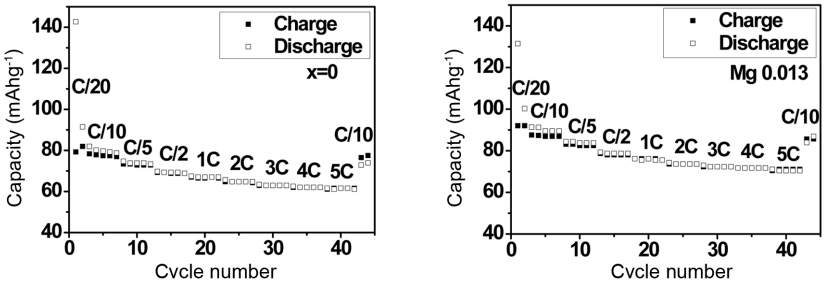

Fig. 9. Rate capability of P2 phases with x = 0 and 0.013.

Acknowledgements

We would like to acknowledge the support of Materials Design (www.materialsdesign.com/medea) and Kyungwon Enc. (www.kwenc.kr), and to thank them for granting us the use of the MedeA-VASP program.

REFERENCES

1. B. Dunn, H. Kamath, and J. Tarascon, "Electrical Energy Storage for the Grid: A Battery of Choices," *Science*, **334** 928-35 (2011).
2. C. D. Wessells, R. A. Huggins, and Y. Cui, "Copper Hexacyanoferrate Battery Electrodes with Long Cycle Life and High Power," *Nat. Commun.*, **2** 550 (2011).
3. M. Pasta, C. D. Wessells, R. A. Huggins, and Y. Cui, "A High-Rate and Long Cycle Life Aqueous Electrolyte Battery for Grid-Scale Energy Storage," *Nat. Commum.,* **3** 1149 (2012).
4. M. Armand and J. M. Tarascon, "Building Better Batteries," *Nature*, **451** 652-57 (2008).
5. L. Suo, Y.-S. Hu, H. Li, M. Armand, and L. Chen, "A New Class If Solvent-In-Salt Electrolyte for High-Energy Rechargeable Metallic Lithium Batteries," *Nat. Commun.*, **4** 1481 (2013).
6. B. L. Ellis, W. R. M. Makahnouk, Y. Makimura, K. Toghill, and L. F. Nazar, "A multifunctional 3.5V Ion-Based Phosphate Cathode for Rechargeable Batteries," *Nat. Mate*r., **6** 749-53 (2007).
7. S.-W. Kim, D.-H. Seo, X. Ma, G. Ceder, and K. Kang, "Electrode Materials for Rechargeable Sodium-Ion Batteries: Potential Alternatives to Current Lithium-Ion Batteries," *Adv. Energy Mater*., **2** 710-21 (2012).
8. A. Hayashi, K. Noi, A. Sakuda, and M. Tatsumisago, "Superionic Glass-Ceramic Electrolytes for Room-Temperature Rechargeable Sodium Batteries," *Nat. Commum.,* **3** 856 (2012).
9. M. D. Slater, D. Kim, E. Lee, and C. S. Johnson, "Sodium-Ion Batteries," *Adv. Funct. Mater*., **23** [8] 947-58 (2013).
10. Y. Lu, L. Wang, J. Cheng, and J. B. Goodenough, "Prussian Blue: A New Framework of Electrode Materials for Sodium Batteries," *Chem. Commun*., **48** 6544-46 (2012).
11. S. Komaba, W. Murata, T. Ishikawa, N. Yabuuchi, T. Ozeki, T. Nakayama, A. Ogata, K. Gotoh, and K. Fujiwara, "Electrochemical Na Insertion and Solid Electrolyte Interphase for Hard-Carbon Electrodes and Application to Na-Ion Batteries," *Adv. Funct. Mater.,* **21** [20] 3859-67 (2011).
12. A. Rudola, K. Saravanan, C. W. Mason, and P. Balaya, "$Na_2Ti_3O_7$: An Intercalation Based Anode for Sodium-Ion Battery Applications," *J. Mater. Chem. A*, **1** 2653-62 (2013).
13. Y. Wang, X. Yu, S. Xu, J. Bai, R. Xiao, Y.-S. Hu, H. Li, X.-Q. Yang, L. Chen, and X. Huang, "A Zero-Strain Layered Metal Oxide as the Negative Electrode for Long-Life Sodium-Ion Batteries," *Nat. Commun*., **4** 2365 (2013).
14. H. Yu, Y. Ren, D. Xiao, S. Guo, Y. Zhu, Y. Qian, L. Gu, and H. Zhou, "An Ultrastable Anode for Long-Life Room-Temperature Sodium-Ion Batteries," *Angew. Chem. Int. Ed.*, **53** 8963-69 (2014).
15 . (a) Y. Mo, S. P. Ong, and G. Ceder, "Insights into Diffusion Mechanisms in P2 Layered Oxide Materials by First-Principles Calculations," *Chem. Mater*., **26** 5208-14 (2014). (b) D. Wu, Xin Li, Bo Xu, N. Twu, L. Liu, and G. Ceder, "$NaTiO_2$: A Layered Anode Material for Sodium-Ion Batteries," *Energy Environ. Sci*., **8** 195-202 (2015).
16. G. V. Shilova, V. B. Nalbandyanb, V. A. Volochaevb, and L. O. Atovmyana, "Crystal Growth and Crystal Structures of the Layered Ionic Conductors–Sodium Lithium Titanium Oxides," *Int. J. Inorganic Mat.,* **2** 443-449 (2000).
17. W. Kohn and L. J. Sham, "Self-Consistent Equations Including Exchange and Correlation Effects," *Phys. Rev. A,* **140** 1133-38 (1965).
18. G. Kresse and J. Furthmuller, "Efficient Iterative Schemes for ab Initio Total Energy Calculations Using a Plane-Wave Basis Set," *Phys. Rev. B*, **54** 11169-86 (1996).
19. Materials Design/MedeA-VASP Program (www.materialsdesign.com/medea)
20. P. E. Blöchl, "Projector Augmented-Wave Method," *Phys. Rev. B*, **50** 17953–79 (1994).
21. J. P. Perdew, K. Burke, and M. Ernzehof, "Generalized Gradient Approximation Made Simple," *Phys. Rev. Lett*., **77** 3865-68 (1996).
22. J. P. Perdew, J. A. Chevary, S. H. Vosko, K. A. Jackson, M. R. Pederson, D. J. Singh, and C. Fiolhais, "Atoms, Molecules, Solids, and Surfaces: Applications of the Generalized Gradient Approximation for Exchange and Correlation," *Phys. Rev. B,* **46** 6671-87 (1992).
23. A. D. Becke, "Density-Functional Thermochemistry. IV. A New Dynamic Correlation Functional and Implications for Exact-Exchange Mixing," *J. Chem. Phys*., **104** 1040-46 (1996).
24. VTST, http://theory.cm.utexas.edu/vtsttools. Accessed on 21/12/2015.
25. K. Momma and F. Izumi, "VESTA: A Three-Dimensional Visualization System for Electronic and Structural Analysis," *J. Appl. Cryst*., **41** 653-68 (2008).